Kinetics and Growth Mechanism of Electrodeposited Palladium Nanocrystallites

Debasis Bera, Suresh C. Kuiry, and Sudipta Seal*

Surface Engineering and Nanotechnology Facility (SNF), Advanced Materials Processing Center (AMPAC) and Mechanical, Materials and Aerospace Engineering (MMAE), University of Central Florida, Eng. 1, Room #381, 4000 Central Florida Boulevard, Orlando, Florida 32816

Received: August 6, 2003; In Final Form: October 21, 2003

Palladium particles have been electrodeposited on AISI 316 stainless steel substrate from aqueous solution of palladium chloride. The kinetics of the electrodeposition process and growth mechanism of such three-dimensionally grown palladium particles have been studied. It has been found that the kinetics of electrodeposition of palladium follows parabolic law, which indicates involvement of instantaneous nucleation and subsequent three-dimensional growth. It was also observed that the nucleation density of palladium electrodeposits was a function of the nature of the electrode substrate. The structure, morphology, texture, chemical state, and composition of the electrodeposited palladium particles have been characterized using SEM, TEM, XPS, EDS, EBSD, and OIM. The growth of the palladium nuclei situated at the grain interior was found to be more than that at the grain boundaries on steel substrate. The micron-size electrodeposited palladium particles consisted of a number of nanocrytallites. The surface morphology of the electrodeposited palladium particles was uneven due to the preferential growth of such nanocrystallites in certain crystallographic directions. The results of the present investigation indicate that the growth of the palladium electrodeposits was limited by the diffusivity of bulky palladium tetrachloro square-planar complex from bulk solution to near the electrode surface.

Introduction

The growing demands in various fields of engineering and technology including catalysis,[1,2] sensors,[3,4] hydrogen storage[5] and separation,[6,7] electronic and optoelectronic devices[8] have stimulated extensive research interest on palladium nanoparticles. Keeping such potential applications in view, numerous studies[2−4,6,9−17] on the nucleation and growth of metallic particles through electrodeposition processes were carried out during past decades. Scharifker et al.[10,11] derived the expressions for current transients for instantaneous and progressive formation of nuclei and their subsequent growth in Pb, Ag, Hg, and Cu systems. Zoval and co-workers[18] used potentiostatic pulse to electrochemically deposit silver nanoparticles on graphite surface. The instantaneous nucleation and three-dimensional growth of Ag particles prevailed, as evidenced[18] from the proportionality of the transient current with the square root of electrodeposition time. In another work, Zoval et al.[14] reported the instantaneous nucleation and diffusion-limited growth of narrowly distributed platinum particles electrodeposited on basal plane of graphite. Electron diffraction investigation[14] revealed that the deposited Pt particles had lattice constants identical to that of the bulk platinum that exhibits face-centered-cubic structure. Moreover, the Pt nanocrystals were not epitaxially oriented on the basal plane of the graphite. Though the electrodeposition of gold on highly oriented pyrolytic graphite was found[13] to follow the same nucleation and diffusional growth processes, the shape of the gold deposit changed from the Euclidean to dendritic fractal morphology due to anisotropic surface diffusion of gold adatoms that was induced by the applied electric field. Barkey et al.[12] investigated the role of interfacial dynamics and anisotropy in electrochemical deposition of Cu on single-crystal electrodes with several surface orientations. They[12] observed that the microscopic interfacial anisotropy in depositional growth stabilizes the dendritic morphology of copper electrodeposits. Amblard and co-workers[19] reported that the preferential orientation of Ni electrodeposits was attributed to the competitive growth as an aftermath of coalescence of hemispherical electrodeposits. The formation of fractal clusters and network during deposition of metal particle under the influence of diffusion-limited aggregation (DLA) was the subject of intense theoretical[20−22] and experimental[23] investigations. Study on the growth kinetics under a steep concentration gradient of diffusing species in the vicinity of the nuclei coupled with electric field assisted diffusion, however, has not been studied to validate the DLA model. A simulation study[24] on the diffusion-controlled growth of metal particles using the Brownian dynamics method strongly indicated the presence of size dispersion even in the case of instantaneous nucleation and growth of particles. Such particle size dispersion was possibly[15] due to the flux inhomogeneity that arises from the varying number of neighbors around the randomly formed instantaneous nuclei. Such nuclei eventually grow and coalesce to give complete coverage of the electrode surface. Tsirlina et al.[16] have used polymers to avoid such coalescence and to promote growth along a preferential direction that controls the size of Pd nanoparticles during electrodeposition. Gimeno and co-workers[2,25] have investigated the electrodeposition of two-dimensional branched Pd islands on highly oriented pyrolitic graphite. The results of such studies[2,25] strongly suggest that the shape and aspect ratio of the palladium island deposits are a function of the cathodic overpotentials. Investigation of the mechanism for nucleation and growth of palladium with the help of electrochemical means by Quayum

* Corresponding author. E-mail: sseal@pegasus.cc.ucf.edu. Phone: 407 882 1119. Fax: 407 882 1462.

10.1021/jp036327e CCC: $27.50
Published on Web 12/10/2003

et al.[17] indicated that the electrodeposition process involved an instantaneous nucleation and subsequent growth.

Preliminary studies on the successful utilization of electrodeposition method to fabricate Pd nanoparticles arrays for hydrogen gas sensing application on previously generated specific templates using laser[4] and nanoindentation[26] are recently reported. However, the kinetics and mechanism of electrodeposition of palladium have not been investigated in these studies.[4,26] The objective of the present investigation was to understand the mechanism of electrodeposition of palladium particles from palladium chloride solution by studying the electrodeposition kinetics. The morphology and texture of the electrodeposited Pd particles constitute the major portion of the present study that was carried out not only to ascertain the nucleation and growth mechanism but also to substantiate the earlier nucleation and growth models[6,10,12,18,19,25] for electrodeposition of metals. The surface morphology and chemical compositions were investigated using scanning electron microcopy (SEM) and energy dispersive spectroscopy (EDS), respectively. The X-ray photoelectron spectroscopy (XPS) study was performed to ascertain the chemical state of the Pd deposits. The crystal structure and the texture of the Pd deposits were evaluated using selected area electron diffraction (SAED) and electron backscattered diffraction (EBSD), which were an integral part of the high-resolution transmission electron microscopy (HRTEM) and orientation imaging microscopy (OIM) systems, respectively. A focused ion beam (FIB) technique was employed to prepare specimens from the Pd electrodeposits for TEM and OIM studies.

Experimental Section

Palladium particles were electrodeposited from aqueous solution of 2.087 mM $PdCl_2$ with 0.1 M hydrochloric acid addition. The solution was prepared using deionized water of specific resistance ~18 MΩ·cm. The electrodeposition was carried out at potential of 0.3 V. An AISI 316 stainless steel rectangular sheet of dimensions 25 mm × 25 mm and 0.5 mm thickness was used as a cathode. The pretreatment included ultrasonic cleaning in acetone followed by distilled and deionized water cleaning. All experiments are carried out at a room temperature of 20 ± 2 °C. Palladium chloride was supplied by Aldrich Chemical Co. with 99% purity. The conventional electrochemical current−time measurements were taken using a flat cell consisting of a three-electrodes assembly that was connected to an EG&G potentiostat (Model: Princeton Instruments 263A). The three electrodes were a steel plate as working electrode, a pure Pt counter electrode and a standard electrode based on saturated Ag/AgCl.

The morphology of the electrodeposited palladium particles was characterized using JEOL T-300 SEM system with an accelerating voltage of 5 and 15 kV for imaging and EDS analysis, respectively. The elemental analysis was carried out using an EDS system attached to the SEM. Specimen preparation for TEM and OIM studies was carried out on focused ion beam equipment (Model: FEI FIB 200TEM) that used a liquid gallium metal ion source in a vacuum of 10^{-9} Torr. A platinum layer was deposited on the surface of Pd particles prior to milling in FIB to avoid specimen damage from the ion beam. The specimen prepared with the help of FIB was subsequently used for an HRTEM (Model: PHILIPS 300 TECNAI) study at 300 kV. The SAED pattern of the Pd particles was also collected from TEM system.

The chemical state of the palladium particles was done using the PHI 5400 ESCA system. The specimen was kept under a vacuum of about 10^{-9} Torr inside the chamber of the XPS system. Nonmonochromatic Mg Kα X-radiation with energy 1253.6 eV at a power of 350 W was used for the analysis. To achieve the maximum resolution, survey and individual high-resolution spectra were recorded with pass energies of 35.7 and 17.9 eV, respectively. The spectrometer was calibrated using a metallic gold standard (Au $4f_{7/2}$ = 84.0 ± 0.1 eV). Charging shifts produced by the sample were removed by using a binding energy scale referenced[27] to that of C(1s) of the hydrocarbon part of the adventitious carbon line at 284.6 eV.

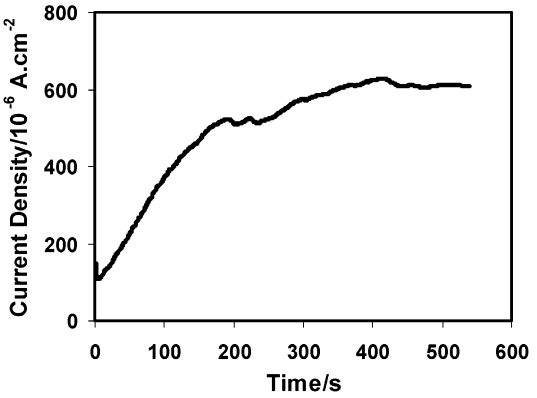

Figure 1. Current density vs time plot for electrodeposition of Pd at 300 mV potential on AISI 316 stainless steel substrate.

An OIM study was conducted at an accelerating voltage of 20 kV on the SEM (Model: Philips XL30) system, which was equipped with a TSL OIM system. The OIM system consisted of a low light sensitive camera, an interface connecting camera to the SEM, and a work station for data collection. The sample surface was oriented 70° with respect to the electron beam during OIM. EBSD data were analyzed using TexSEM OIM data analysis software. A thin sample was freshly prepared using FIB and placed under SEM to capture the grain map. The OIM map was obtained with a step size of 10 nm that revealed information to understand the microstructure, texture, and crystallographic relationships of grains in three dimensions. The OIM map allows for visual representation of the microstructure in a format that reveals crystallographic orientation and grain boundaries.[28,29]

Results and Discussion

Figure 1 depicts the current−time plot of electrodeposition of palladium at 300 mV. It shows a sharp drop in current density at the beginning due to the charging of the double layer, which was followed by a nonlinear increase of the current density with electrodeposition time. Such double layer charging was also observed[10,13,18] during electrodeposition of various metals. Figure 2 presents the log(current density) vs log(time) of electrodeposition of the corresponding data presented in Figure 1. The slope of the log−log plot in Figure 2 is 0.5, which indicates that the electrodeposition kinetic follows a parabolic relationship. Similar parabolic kinetics of electrodeposition of metallic nanoparticles was also observed by others.[2,13,14,17,18,25] The parabolic relationship of the current density with deposition time indicates a process of instantaneous nucleation and subsequent three-dimensional growth of such nuclei having hemispherical shape. The value of the parabolic rate constant (k_P) that was obtained from the slope of current density vs $t^{1/2}$ plot of data presented in Figure 1, was 3.06×10^{-5} A·cm^{-2}·s$^{-1/2}$. The electrodepo-

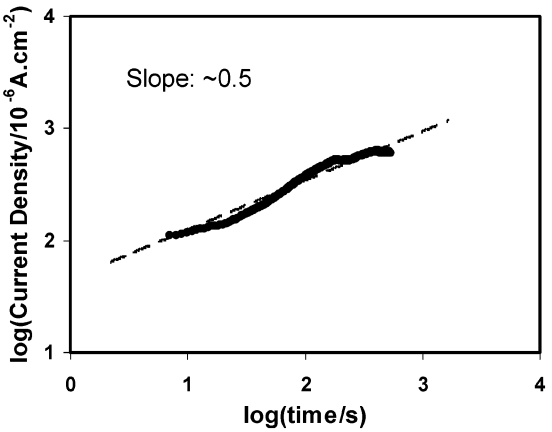

Figure 2. log(current density) vs log(time) plot for electrodeposition of Pd at 300 mV potential on AISI 316 stainless steel substrate.

sition current (I) usually obeys the following growth relation:[9,10]

$$I = \frac{zF\pi(2Dc)^{3/2}M^{1/2}Nt^{1/2}}{\rho^{1/2}} \quad (1)$$

where D is the diffusion coefficient, c is the concentration of metallic ions in the solution, zF is the effective molar charge of the electrodepositing species, t is time, and N is the number density of nuclei. M and ρ are the molecular weight and density of the metallic species deposited, respectively. Therefore, the experimentally found out value of k_P can be utilized to estimate the number density of instantaneous Pd nuclei formed in the present study by using the following relation:

$$N = \frac{\rho^{1/2}}{zF\pi(2Dc)^{3/2}M^{1/2}}k_P \quad (2)$$

Taking the values of $z = 2$, $F = 96500$ Coulomb·mol^{-1}, $D = 6.70 \times 10^{-6}$ cm^2·s^{-1},[25] $M = 106.42$ g·mol^{-1}, $c = 2.087 \times 10^{-6}$ mol·cm^{-3}, and $\rho = 12.023$ g·cm^{-3} and using the experimentally found out values of k_P as 3.06×10^{-5} A·cm^{-2}·s$^{-1/2}$, the N was found to be 1.146×10^5 cm^{-2}. The values of the N estimated for electrodeposition of Pd in experimental conditions other than the present situation have been reported[2,25] to be 5.8×10^9 and 3.6×10^8 cm^{-2}, indicating a difference of a few orders of magnitude. Such a discrepancy is probably attributed not only to the choice of cathode substrate but also to electrochemical parameters such as concentration of Pd ions and potential. The substrate used in the earlier studies[2,25] for deposition of Pd was highly oriented pyrolitic graphite, whereas AISI 316 stainless steel was used in the present investigation.

SEM micrographs showing the Pd electrodeposits on the AISI 316 stainless steel substrate at 300 mV for 180 s is depicted in Figure 3a. Figure 3a confirms the presence of small Pd particles in the size range of 50−100 nm along with large deposits in the size range 700−1000 nm. The deposited large Pd particles do not reveal a smooth and faceted surface, rather a preferential growth along certain directions. Moreover, the Pd particles exhibit a bimodal particle size distribution indicating that the growth rate of particles at some preferential locations was more than that of the others. The EDS spectrum taken from the surface of the Pd-deposited steel plate is depicted in Figure 3b, which confirms that those particles on the steel surface are of Pd. Figure 3c is the EDS spectrum of stainless steel before deposition revealed the presence of Fe, Cr, Ni, and Mo, which were from the steel substrate. To confirm the chemical state of

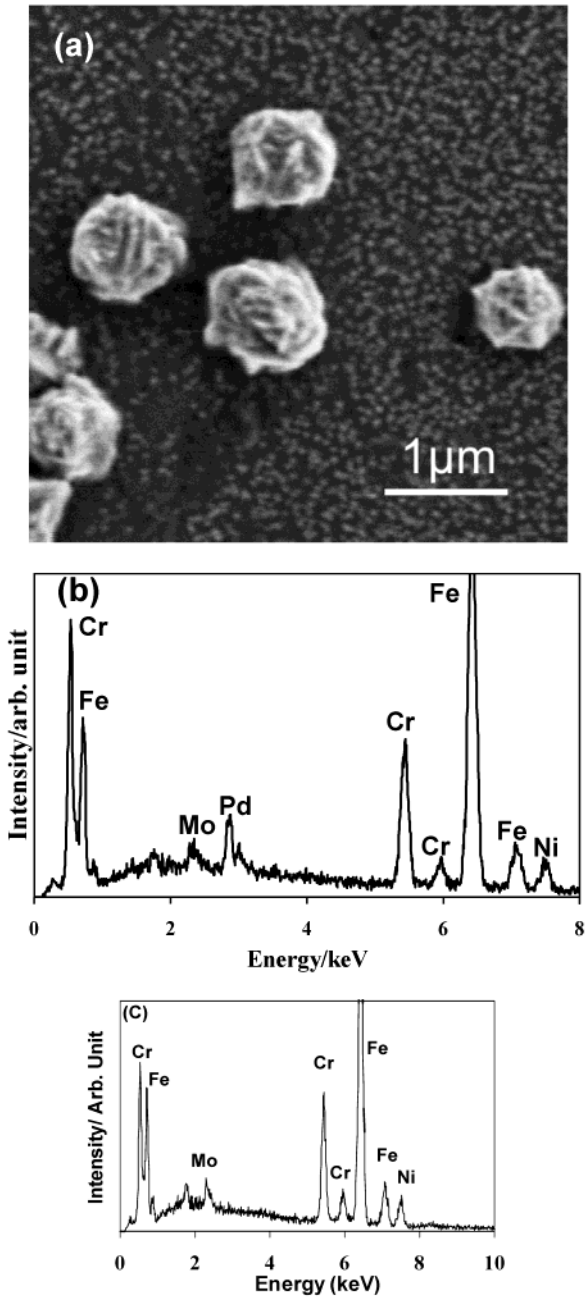

Figure 3. (a) SEM micrograph of Pd electrodeposits on AISI 316 stainless steel substrate at 300 mV for 180 s and (b) corresponding EDS spectrum. (c) EDS spectrum of stainless steel before deposition.

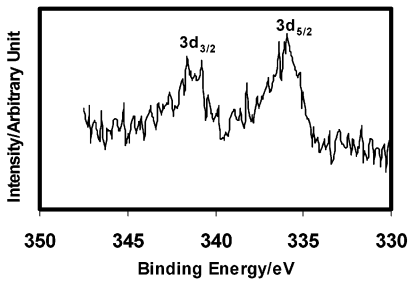

Figure 4. XPS Pd(3d) envelope of metallic Pd electrodeposits on AISI 316 stainless steel substrate at 300 mV for 180 s.

the palladium particles, XPS study was carried out. XPS spectrum of Pd(3d) envelope is shown in Figure 4, which revealed the presence of Pd($3d_{5/2}$) and Pd($3d_{3/2}$) peaks at binding

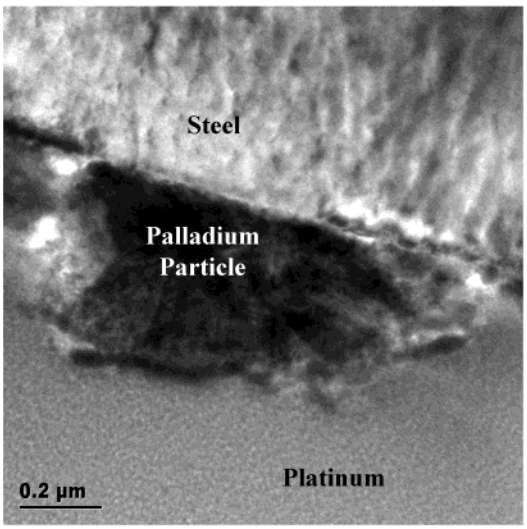

Figure 5. TEM bright-field image showing the cross section of a Pd electrodeposit and steel substrate prepared using FIB.

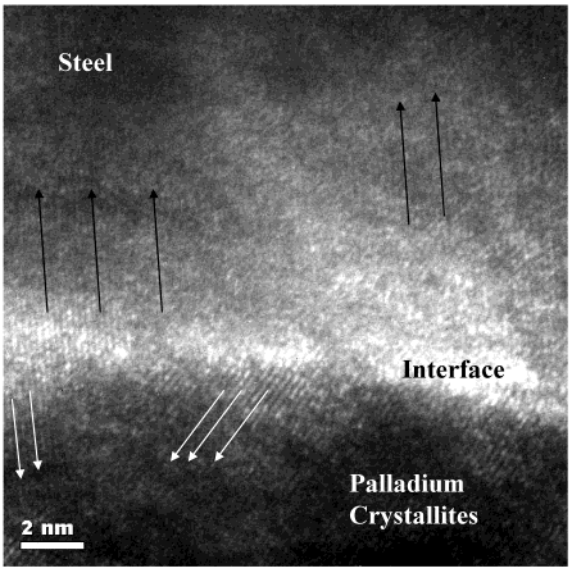

Figure 6. HRTEM image taken from near the Pd−steel interface. Arrows are provided to show the orientation of lattice fringes.

energy values of 335.9 and 341.2 eV, respectively. Such binding energy values are similar to that reported for metallic Pd in the literature.[30]

A TEM bright-field image showing the cross section of a Pd particle prepared using FIB is presented in Figure 5. The shape of the deposited Pd particle was hemispherical. Figure 6 presents the HRTEM image taken from near the Pd−steel interface, which reveals the presence of Pd nanocrystallites. The lattice fringes of the steel substrate as well as that of the palladium electrodeposit are visible in the HRTEM image (Figure 6). Although the Pd particle was electrodeposited on one grain of the steel substrate, the Pd crystallites exhibited more than one orientation of the lattice fringes. Perhaps the rate of growth of the crystallites, those electrodeposited with a certain crystallographic direction, was more favorable compared to others. Consequently, such growth behavior yielded a nonuniform size distribution, as shown in Figure 3a. The SAED pattern taken from an area covering the Pd particle and the steel substrate is shown in Figure 7, which reveals the presence of bright diffraction spots along with diffraction rings. The presence of such rings suggests that the Pd particle consisted of Pd

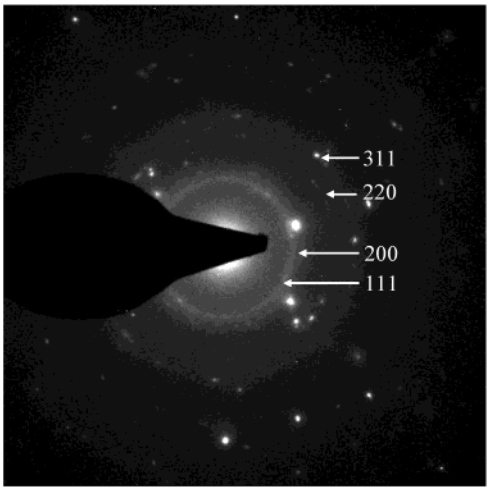

Figure 7. Indexed SAED pattern taken from an area covering the Pd particle as shown in Figure 5 and the stainless steel substrate.

nanocrystallites. After indexing, the bright diffraction spots were confirmed to be from the steel grain on which the Pd particle was electrodeposited. To reveal the grain boundaries of the steel substrate, bare and Pd electrodeposited steel specimens were thermally etched by heating inside an electrically heated tube furnace in an argon atmosphere. SEM micrographs of bare and Pd-deposited steel surface after thermal etching are shown in Figure 8a,b, respectively. The grain boundaries of the steel substrate are clearly revealed in Figure 8a after thermal etching. The grain size of the steel substrate was in the range of 10−15 μm. It can be mentioned that the steel plate was annealed at 770 °C for 2 h in an argon atmosphere followed by a slow cooling up to room temperature. It is quite likely that chromium carbide was precipitated[31] along the grain boundaries during such a slow cooling stage, which helps reveal the grain boundaries under the SEM. These carbide particles have low electrical conductivity and hence charging occurs as the electron beam interacted with the carbide particles. The formation of nuclei at the grain boundaries was easy due to the abundance of two-dimensional defects that act as preferential nucleation sites. Stainless steel usually forms a very thin and impervious Cr−oxide layer at room temperature. The thickness of such an oxide layer is expected to be more on the grain boundaries. Usually, the nucleation process during electrodeposition, in such situation, is easier. However, the further growth of the nuclei may be limited at grain boundaries due to the lower electrical conductivity. Figure 8b indicates such growth behavior of Pd nuclei. The growth rate of the Pd particles situated on the grain interior was more than those deposited at the grain boundaries to the difference in the electrical conductivity values of the grain interior and the grain boundaries.

The palladium particle with preferential growth along certain directions, as shown in Figure 3a, was investigated in OIM to study the orientation of such growth directions. Orientation imaging microscopy has been used to analyze the local texture and grain boundary structure of the Pd particle by rapidly capturing and processing EBSD patterns. An EBSD pattern taken from the Pd particle is shown in Figure 9. The SEM micrograph of the Pd particle from which the EBSD pattern was obtained is shown as the left-bottom inset of Figure 9. It may be mentioned that the Pd particle was sandwiched between the protective Pt layer and the stainless steel substrate. The crisscrossing Kikuchi lines originating from various planes along with their zone axes were indexed. The indices of each plane are indicated in the color legend at the top-left corner of Figure

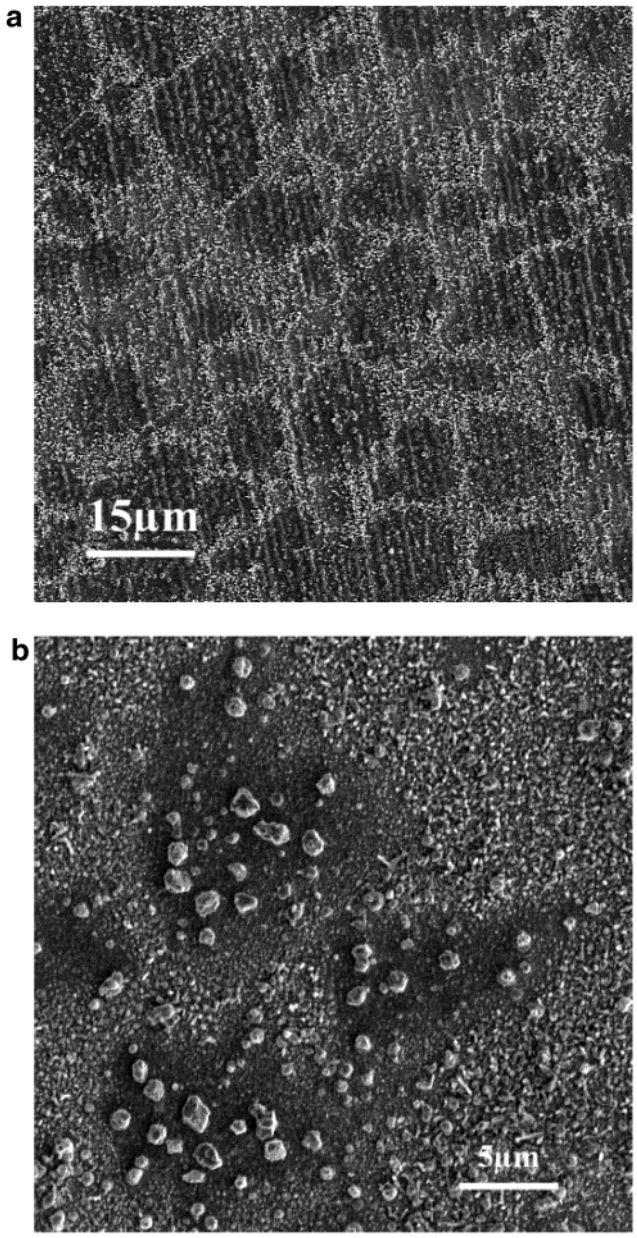

Figure 8. SEM micrographs of (a) the bare and (b) the Pd-deposited stainless steel surface after thermal etching.

9. The OIM system carried out a large number of orientation measurements in a very short time by linking the local lattice orientation with the grain morphology of the Pd deposits. The OIM image of a Pd particle is shown in Figure 10 which reveals that the Pd particle consisted of a number of nanocrystallites. The size distribution of the Pd nanocrystallites was obtained from the OIM study, which is shown in Figure 11. The mean size of the nanocrystallites is 140 nm and about 60% of the total nanocrystallites present in that Pd electrodeposit were in the size range of less than 100 nm.

It may be mentioned that the SAED pattern (Figure 7) exhibited the presence of diffraction rings, which was attributed to the presence of such nanocrystallites. The OIM study (Figure 11) confirms the results of the SAED analysis. The tiny crystallites have grown along the preferential direction during electrodeposition. Such uneven growth possibly led to the formation of a rough surface morphology on the spherical Pd particles, as observed in the SEM micrograph (Figure 3a). The inset of Figure 10 depicts the single stereographic triangle showing the orientation of the various nanocrystallites. It can

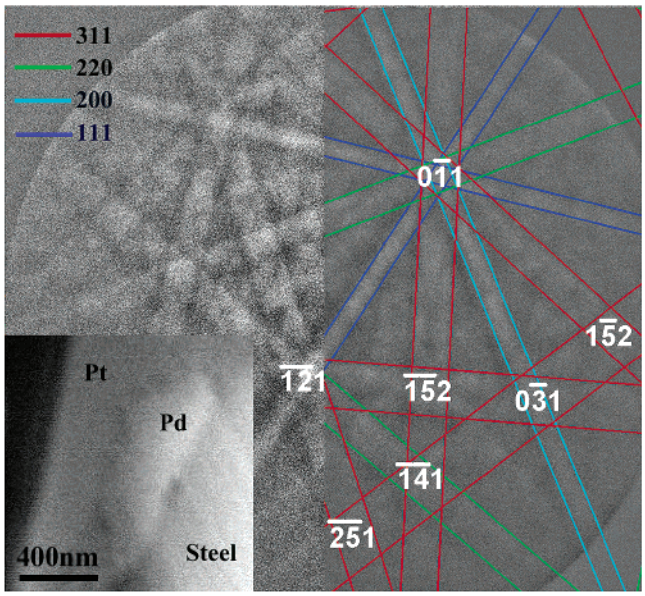

Figure 9. SEM micrograph (left bottom inset) of the EBSD (Kikuchi) pattern taken from the Pd particle. The color legend indicates the FCC lattice planes. Zone axes are indicated in the figure.

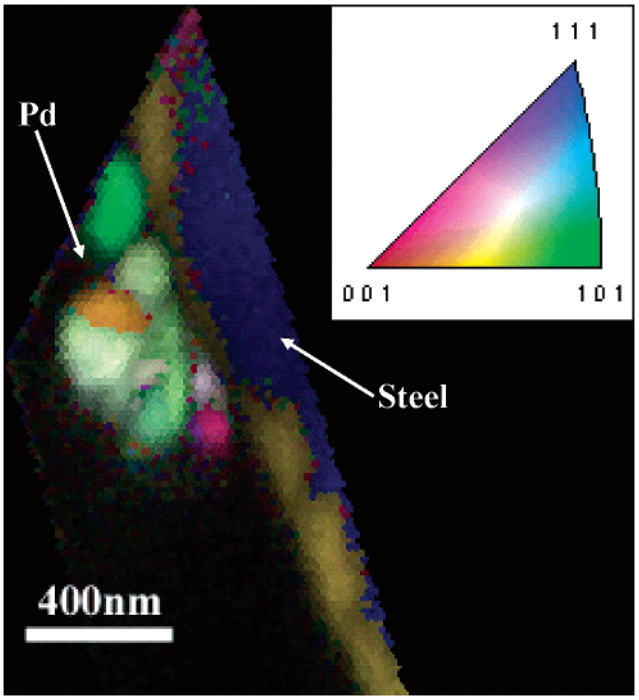

Figure 10. OIM image of the Pd crystallites electrodeposited on the steel substrate and the single stereographic triangle (inset).

be seen that the growth of the Pd crystallites took place in some preferential crystallographic direction during the electrodeposition of Pd from the solution. Figure 10 further reveals that the Pd particles have grown preferentially on the grain interior of the steel substrate and not on the grain boundary. Such preferential growth on the grain interior was also observed in SEM study after thermal etching (Figure 8b) and in HRTEM investigation (Figure 6).

Mechanism of Electrodeposition of Pd

Results of the present investigation indicate that the palladium nuclei formed on the surface of the steel plate during electrodeposition. It is well-known that nucleation occurs prefer-

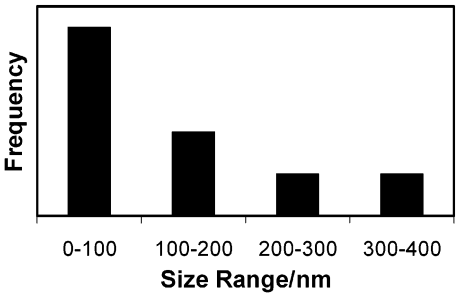

Figure 11. Particle size distribution of palladium nanocrystallites obtained from OIM data.

entially at the holes or disorder state of the substrate on which the metal is to be deposited.[4,26] Although nucleation occurred preferentially at the grain boundaries, the extensive growth took place only for nuclei that were situated on the grain interior, as shown in Figure 8b. The probable reason for such discrepancy in deposition of palladium particles on the grain rather than on the grain boundary is the presence of oxide ridges at the grain boundaries where the formation of Cr−oxide is easy at room temperature. Stainless steel consists of 18 wt % chromium, which oxidizes at room temperature and forms a thin film on the surface of the substrate. The oxidation process is more favorable at the grain boundaries because the formation of oxide nuclei at room temperature is energetically more favored due to the presence of defects. Therefore, instead of continuous deposition throughout the surface of the steel plate, the deposition took place at certain locations. Prior to the initiation of electrodeposition, palladium chloride forms $[PdCl_4]^{2-}$, palladium tetrachloro square-planar complex in hydrochloric acid medium, as per the following reaction:[32]

$$PdCl_2 + 2Cl^- = [PdCl_4]^{2-} \quad (3)$$

The electrode reaction starts right after formation and charging of the double layer of hydronium ion (H_3O^+) and $[PdCl_4]^{2-}$ on the steel electrode. During the charging period, the current density decreases sharply with time, which has been shown in the current−time trace in Figure 1. The succeeding part exhibited a rise of current with the increase of electroactive area, indicating a progressive growth of the nuclei with time. Considering the double layer of charge on the cathode, the reduction process of palladium ions may be explained through an inner-sphere mechanism.[33] The palladium ions in the form of $[PdCl_4]^{2-}$ are possibly reduced by accepting electrons from the electrode through hydrogen-bonded hydronium ion. The mechanism of such electron transfer is schematically shown in Figure 12. The reduction mechanism of $[PdCl_4]^{2-}$ to atomic palladium (Pd^0) is complicated and it was speculated[2] to consist of several steps involving $[PdCl_3]^-$, $[PdCl_2]$, and $[PdCl]^+$ species. However, it is not clear whether the complete reduction of $[PdCl_4]^{2-}$ involved a number of steps or all four Cl^- ions were released simultaneously through the inner-sphere mechanism. Usually, $[PdCl_4]^{2-}$ is a square-planar complex and the electron transfer for simultaneous release of all four Cl^- ions is highly likely. Nevertheless, the overall discharge of metallic palladium to the steel cathode from the $[PdCl_4]^{2-}$ species in the solution may be expressed as follows:

$$[PdCl_4]^{2-} + 2e^- = Pd^0 + 4Cl^- \quad (4)$$

Successive discharge of Pd atoms forms the nuclei on the surface of the steel electrode. According to classical nucleation theory,[34,35] as soon as a nucleus has reached the critical size, it starts growing by incorporating additional atoms. The free energy of formation (ΔG) of a hemispherical embryo[36] with radius r may be written as

$$\Delta G = \frac{2}{3}\pi r^3 \Delta G_v + 2\pi r^2 \gamma \quad (5)$$

where ΔG_v is the volume free energy change associated with transfer of Pd atoms from solution to the steel substrate, which is negative. The term γ is the surface energy between the palladium particle and the stainless steel plate, which is a monotonically increasing function with the size of the embryo. The overall free energy change is expected to increase till a critical value of radius, where the embryo would turn into a nucleus. Further growth of such a nucleus beyond the critical size is feasible because ΔG is negative.

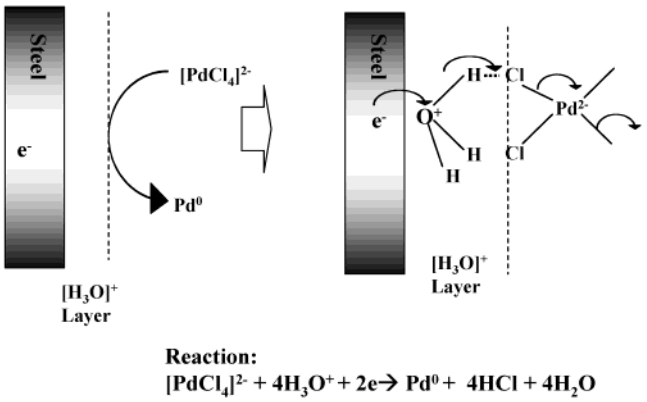

Figure 12. Reduction mechanism of palladium chloride to metallic Pd.

With the further progress of the electrodeposition, Pd atoms were continuously deposited on the surface of the nuclei. Because the electrode is negative in charge, the hydronium ion will be attracted toward the electrode, forming a positive hemispherical layer on the freshly deposited palladium particles followed by a negative layer of $[PdCl_4]^{2-}$, as shown in Figure 12. Such continuous deposition of Pd is expected to go on until the palladium ion concentration is depleted near the deposits. Consequently, the Pd deposition process ceases. To continue the Pd reduction process, a supply of $[PdCl_4]^{2-}$ ions from the bulk solution to near the cathode is required. However, the migration of $[PdCl_4]^{2-}$ ions toward the electrode is a difficult process because of its inherently bulky structure. Consequently, the current density is limited by the diffusivity of palladium ions through the negatively charged interface.

Conclusions

1. The kinetics of electrodeposition of palladium follows parabolic law, which indicates instantaneous nucleation and subsequent three-dimensional growth process.

2. The nucleation density depends on the nature of the electrode substrate. The growth of the palladium nuclei situated at the grain interior is more than that at the grain boundaries on AISI 316 stainless steel substrate.

3. The electrodeposited palladium particles consisted of a number of nanocrytallites. The surface morphology of the electrodeposited palladium particles is uneven due to the preferential growth of the nanocrystallites in certain crystallographic direction.

4. The growth of the palladium electrodeposits is limited by the diffusivity of $[PdCl_4]^{2-}$ ions from bulk to near the electrode surface.

Acknowledgment. We thank the NSF (grant EEC 0136710, 0085639), FSEC-NASA Glenn, FL, Space Grant Consortium, and MCF facilities at AMPAC, UCF, Orlando, for financial and equipment support.

Supporting Information Available: STEM picture of FIB cut palladium deposit and EDX spectrum from the identified area of the STEM image. This material is available free of charge via the Internet at http://pubs.acs.org.

References and Notes

(1) Diaz, R.; Arbiol, J.; Cirera, A.; Sanz, F.; Peiro, F.; Cornet, A.; Morante, J. R. *Chem. Mater.* **2001**, *13*, 4362.
(2) Gimeno, Y.; Creus, A. H.; González, S.; Salvarezza, R. C.; Arvia, A. J. *Chem. Mater.* **2001**, *13*, 1857.
(3) Favier, F.; Walter, E. C.; Zach, M. P.; Benter, T.; Penner, R. M. *Science* **2001**, *293*, 2227.
(4) Bera, D.; Kuiry, S. C.; Patil, S.; Seal, S. *Appl. Phys. Lett.* **2003**, *82*, 3089.
(5) Bemis, J. M.; Dahl, L. F. *J. Am. Chem. Soc.* **1997**, *119*, 4545.
(6) Bryden, K. J.; Ying, J. Y. *J. Electrochem. Soc.* **1998**, *145*, 3339.
(7) Bryden, K. J.; Ying, J. Y. *J. Membr. Sci.* **2002**, *29*, 203.
(8) Walter, E. C.; Ng, K.; Zach, M. P.; Penner, R. M.; Favier, F. *Microelectron. Eng.* **2002**, *61*−*62*, 555.
(9) Gunawardena, G.; Hills, G.; Montenegro, I.; Scharifkar, B. *J. Electroanal. Chem.* **1982**, *138*, 225.
(10) Scharifker, B.; Hills, G. *Electrochim. Acta* **1983**, *28*, 879.
(11) Hills, G.; Pour, A. K.; Scharifker, B. *Electrochim. Acta* **1983**, *28*, 891.
(12) Barkey, D.; Oberholtzer, F.; Wu, Q. *Phys. Rev. Lett.* **1995**, *75*, 2980.
(13) Martin, H.; Carro, P.; Creus, A. H.; González, S.; Salvarezza, R. C.; Arvia, A. J. *Langmuir* **1997**, *13*, 100.
(14) Joval, J. V.; Lee, J.; Gorer, S.; Penner, R. M. *J. Phys. Chem. B* **1998**, *102*, 1166.
(15) Zach, M. P.; Penner, R. M. *Adv. Mater.* **2000**, *12*, 878.
(16) Tsirlina, G. A.; Petrii, O. A.; Safonova, T. Y.; Papisov, I. M.; Vassiliev, S. Y.; Gabrielov, A. E. *Electrochim. Acta* **2002**, *47*, 3749.
(17) Quayum, M. E.; Ye, S.; Uosaki, K. *J. Electroanal. Chem.* **2002**, *520*, 126.
(18) Joval, J. V.; Stiger, R. M.; Biernacki, P. R.; Penner, R. M. *J. Phys. Chem.* **1996**, *100*, 837.
(19) Amblard, J.; Froment, M.; Maurin, G.; Spyrellis, N.; Trevisan-Souteyrand, E. *Electrochim. Acta* **1983**, *28*, 909.
(20) Witten, T. A., Jr.; Sander, L. M. *Phys. Rev. Lett.* **1981**, *47*, 1400.
(21) Witten, T. A., Jr.; Sander, L. M. *Phys. Rev. B* **1983**, *27*, 5686.
(22) Meakin, P. *Phys. Rev. Lett.* **1983**, *51*, 1119.
(23) Hwang, R. Q.; Schröder, J.; Günther, C.; Behm, R. J. *Phys. Rev. Lett.* **1991**, *67*, 3279.
(24) Fransaer J. L.; Penner, R. M. *J. Phys. Chem. B* **1999**, *103*, 7643.
(25) Gimeno, Y.; Creus, A. H.; Carro, P.; González, S.; Salvarezza, R. C.; Arvia, A. J. *J. Phys. Chem. B* **2002**, *106*, 4232.
(26) Carrey, J.; Bouzehouane, K.; George, J. M.; Ceneray, C.; Blon, T.; Bibes, M.; Varuès, A.; Fusil, S.; Kenane, S.; Vila, L.; Piraux, L. *Appl. Phys. Lett.* **2002**, *81*, 760.
(27) Barr, T. L.; Seal, S. *J. Vac. Sci. Technol.* **1995**, *A13*, 1239.
(28) Adams, B. L.; Wright, S. I.; Kunze, K. *Metall. Trans. A.* **1993**, *24A*, 819.
(29) Matteson, T. L.; Schwarz, S. M.; Houge, E. C.; Kempshall, B. W.; Gianuzzi, L. A. *J. Electron. Mater.* **2002**, *31*, 33.
(30) Moulder, J. F.; Stickle, W. F.; Sobol, P. E.; Bomben, K. D. In *Handbook of X-ray Photoelectron Spectroscopy*; Chastain J., Ed.; Physical Electronics Division, Perkin-Elmer Corp.: Eden Prairie, Minnesota, 1984.
(31) Hall, E. L.; Briant, C. L. *Metall. Trans. A* **1984**, *14*, 793.
(32) Droll, H. A.; Block, B. P.; Fernelius, W. C. *J. Phys. Chem.* **1957**, *61*, 1000.
(33) McCeery, R. L. In *Interfacial Electrochemistry: Theory, Experiment and Application*; Wieckowski, A., Ed.; Marcel Dekker: New York, 1999.
(34) Volmer, M.; Weber, A. *Z. Phys. Chem., Stoechiom. Verwandtschaftsl.* **1926**, *119*, 277.
(35) Becker, R.; Doring, W. *Ann. Phys.* **1935**, *24*, 719.
(36) Reed-Hill, R. E.; Abbaschian, R. *Physical Metallurgy Principles*; PWS Publishing Co.: Boston, 1994.